INORGANIC CHEMISTRY FRONTIERS

RESEARCH ARTICLE

View Article Online
View Journal | View Issue

Cite this: *Inorg. Chem. Front.*, 2023, **10**, 6221

Efficient iodine capture by metal–organic cubes based on hexanuclear vanadium clusters†

Yang Yang,[a] Yaomei Fu,[b] Yiran Tian,[a] Liang Zhao,*[a] Chao Qin,[a] Xinlong Wang *[a,c] and Zhongmin Su[a,c]

Received 31st July 2023,
Accepted 2nd September 2023

DOI: 10.1039/d3qi01501g

rsc.li/frontiers-inorganic

The cube is the only regular hexahedron among the Platonic solids, but supramolecules with a cubic configuration have rarely been reported. Herein, two isostructural metal–organic cubes **VMOC-6** and **VMOC-7** with large cavities are successfully synthesized by face-directed self-assembly of concave hexanuclear vanadium clusters $[V_6O_6(OCH_3)_9(XO_4)(COO)_3]^{n-}$ (X = S, n = 2; X = V, n = 1) and large-size nitrogen-containing tetravalent ligands. **VMOC-6** and **VMOC-7** are the largest metal–organic cubes based on metal clusters with an outer diameter of 28.47 × 28.17 × 28.44 Å^3 and an inner cavity volume of 7785.657 Å^3. Moreover, the cages can capture volatile iodine vapor with an uptake value of up to 1.83 g g^{-1}, which is superior to those of most metal–organic materials. Mechanistic studies have shown that their good adsorption capacity is closely related to the presence of large internal cavities, electron-donating pyridine groups and redox-active V sites. The present work shows the potential application of these mesoporous MOPs in the treatment of iodine-containing nuclear waste.

Introduction

Self-assembly processes driven by non-covalent interactions are essential in the proliferation of all biological organisms and offer considerable advantages in the construction of large supramolecular assemblies.[1–6] Metal–organic polyhedra (MOPs or molecular coordination cages) constructed by coordination-driven self-assembly processes not only are aesthetically attractive but also have attracted widespread interest due to their large inner cavities and controlled cavity environments, which allow them to be used as advanced functional materials for molecular recognition, catalysis, and optoelectronics applications.[7–13] Unlike metal–organic frameworks (MOFs), MOPs are closed discrete structures, and their assembly process requires strict consideration of the harmony of chemical complementarity and spatial compatibility between organic and inorganic building units.[14,15] Therefore, the design and assembly of MOPs with large internal cavities and potential functions remains one of the challenges in the field of supramolecular chemistry and materials science.

The cube is the only regular hexahedron among the Platonic solids, consisting of congruent regular squares with three meeting at each vertex. In addition, the cube is the only zonohedron with high symmetry consisting of an even number of side faces, and only a few supramolecules with a cubic configuration have been reported.[16–19] To design and construct a molecular cube, at least three conditions must be satisfied: (i) the inorganic building block of the vertex must be trivalent; in other words, it can act as a "3-pyramidal" molecular building block (MBB); (ii) the angle η between the links in the MBB must be close to the desired ideal value, close to 90° for edge-directed models and should be close to 60° for face-directed models; (iii) eight "3-pyramidal" MBBs and the organic building blocks should be assembled into a closed shape arranged in a V_8E_{12} or V_8F_6 geometry (V, E, and F denote vertices, edges and faces, respectively).[19] In other words, the cube can consist of eight identical "3-pyramidal" MBBs connected by twelve "2-linear" or six "4-planar" ligands (Fig. 1).

Therefore, we reasoned that it is easier to construct closed polyhedra from directional metal clusters than from individual metal ions due to their abundant geometric properties. In recent years, we have been investigating polyoxovanadate-based metal–organic polyhedra and have demonstrated that polyoxovanadates are a good category of molecular building blocks (MBBs) for the construction of MOPs, including $[V_6O_6(OCH_3)_9(SO_4)_4]_5$ ($\{V_6(SO_4)_4\}$), $[V_5O_9Cl]_6$, and

[a]*Key Laboratory of Polyoxometalate and Reticular Material Chemistry of Ministry of Education, Northeast Normal University, Changchun, 130024, China. E-mail: zhaol352@nenu.edu.cn, wangxl824@nenu.edu.cn*
[b]*Shandong Peninsula Engineering Research Center of Comprehensive Brine Utilization, Weifang University of Science and Technology, Shouguang, 262700, China*
[c]*College of Science, Hainan University, Haikou 570228, China*

†Electronic supplementary information (ESI) available: Additional characterization data, including ^{1}H NMR spectra, single-crystal X-ray diffraction data, IR spectra, TGA curves, PXRD patterns and UV-vis spectra. CCDC 2278526 and 2278527. For ESI and crystallographic data in CIF or other electronic format see DOI: https://doi.org/10.1039/d3qi01501g

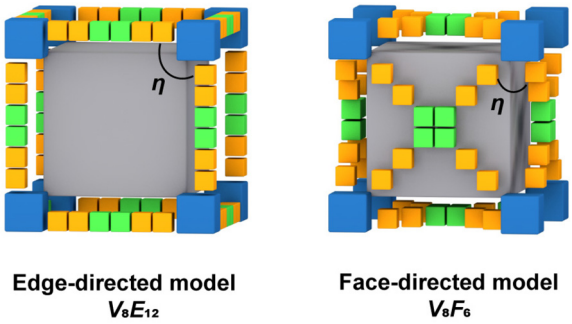

Fig. 1 Schematic diagram of the cube construction guided by edge-directed (left) and face-directed (right) strategies.

$[WV_5O_{11}(SO_4)_6]_8$.[20–25] All these concave MBBs are favorable for the construction of isolated polyhedra, but only the 3-connected $\{V_6(SO_4)_4\}$ satisfies the conditions for the construction of cubes. However, in the process of trying to design MOPs with such building blocks, most of the edge-directed strategies are used as guiding principles to obtain MOPs with tetrahedral configurations.[20,24,26,27] Because of the rigidity limitation of this MBB itself, it is difficult to reach an η angle of 90°, so it also seems to be difficult to construct cubes using the edge-directed strategy. As confirmed by our previous studies, it is possible to obtain a cubic structure by guiding through a face-directed strategy, since the η angle is 60° at this point.[28] A series of polyoxovanadate-based metal–organic cubes constructed from three-coordinated $\{V_6(SO_4)(CO_2)_3\}$ and tetracarboxylic acid ligands of different lengths and of C_4-symmetry have been obtained. The size of the cubic cage can be adjusted by changing the ligand spacer portion while keeping the structural topology unchanged. We found that in these structures, the length of the four ligands is a key determinant of the size of the cubic cage. However, increasing the length of the ligands did not increase the cage size, and the side length of the largest **VMOC-4** increased by only 0.35 Å compared to the smallest **VMOC-1**. Therefore, in this work, wider 4,4′,4″,4″-(1,4-phenylbis(pyridine-4,2,6-triyl))tetrabenzoic acid (H_4PBPTA) was designed as a tetra-connected organic ligand, which was assembled with three-connected $\{V_6O_6(OCH_3)_9(SO_4)\}$ or $\{V_6O_6(OCH_3)_9(VO_4)\}$ into two isomorphic cubic cages **VMOC-6** and **VMOC-7** with large size cavities and with side lengths of about 28.36 Å. In addition, their large cavities, electron-donating pyridine groups and redox-active V sites enable them to exhibit excellent performance in iodine capture.

Experiments and methods

Synthesis of $(NH_2Me_2)_{16}[(V_6O_6(OCH_3)_9(SO_4))_8(PBPTA)_6]$ (VMOC-6). $VOSO_4{\cdot}xH_2O$ (0.02 g, 0.12 mmol) and H_4PBPTA (0.01 g, 0.03 mmol) were dissolved in 0.5 mL of *N*,*N*-dimethylformamide (DMF) and 2.5 mL of methanol (MeOH). The mixed solution was transferred to a reaction vessel and heated to 160 °C for 48 hours. After cooling to room temperature, green rectangular crystals were obtained by filtration. Yield: 40%. Elemental analysis (%): calcd for $C_{368}H_{490}N_{28}O_{200}S_8V_{48}$: C, 39.44; H, 4.41; N, 3.50; found: C, 39.18; H, 4.56; N, 3.25. IR (KBr, cm^{-1}): 3511 (br), 3441 (m), 3385 (m), 3035 (m), 2930 (m), 2810 (m), 1711 (m), 1655 (vs), 1600 (s), 1550 (s), 1480 (s), 1403 (vs), 1242 (m),1172 (m), 1095 (m), 1067 (m), 955 (vs), 864 (m), 829 (m), 780 (m), 696 (m), 668 (m), 577 (s), 542 (s).

Synthesis of $(NH_2Me_2)_{24}[(V_6O_6(OCH_3)_9(VO_4))_8(PBPTA)_6]$ (VMOC-7). $VOSO_4{\cdot}xH_2O$ was replaced with $VO(acac)_2$ (0.02 g, 0.07 mmol) in the above-mentioned procedure and other conditions were kept constant. Brown streaky crystals were obtained in 45% yield. Elemental analysis (%): calcd for $C_{384}H_{544}N_{36}O_{200}V_{56}$: C, 39.36; H, 4.68; N, 4.30; found: C, 39.18; H, 4.46; N, 4.54. IR (KBr, cm^{-1}): 3595 (br), 3518 (m), 3441 (m), 3363 (m), 3028 (m), 2915 (m), 2818 (m), 1711 (m), 1663 (s), 1600 (vs), 1550 (s), 1487 (s), 1403 (vs), 1312 (m), 1249 (s), 1179 (m), 1060 (s), 1018 (s), 984 (s), 948 (vs), 871 (s), 836 (s), 780 (s), 745 (m), 703 (m), 668 (s), 535 (s).

Results and discussion

Structural description

The strong acidity of vanadium has led to the preferential use of oxygen-donating ligands for the construction of vanadium-based metal–organic materials.[29,30] In previous work, a series of metal–organic cubes were constructed by self-assembly of $\{V_6S\}$ with H_4BPTC and its derived tetradentate carboxylic acid ligands. These ligands have equal distances between adjacent carboxyl groups at both ends and have the same width. The length of the ligands is adjusted by changing the middle spacing portion of the ligands, thus adjusting the size of the cubic cage, where the longest ligand, tris-biphenyl-3,3′,5,5′-tetracarboxylic acid (H_4TCTP), constitutes the largest cubic cage. Therefore, to obtain a larger cubic cage, we chose to increase the width of the ligand while keeping the maximum length unchanged, *i.e.*, by replacing the adjacent carboxylic acid at both ends of the original ligand with benzoic acid, as the addition of the benzene ring broadens the distance between the adjacent carboxyl groups. The larger tetracarboxylic acid ligand H_4PBPTA was synthesized (Fig. S1†), and the metal–organic cubes **VMOC-6** and **VMOC-7** with the same configuration were successfully obtained by reactions with $VOSO_4$ and $VO(acac)_2$, respectively. Thermogravimetric analysis and infrared spectral characterization of both are shown in Fig. S2 and S3.† Single-crystal X-ray diffraction analysis shows that both **VMOC-6** and **VMOC-7** crystallize in the triclinic space group $P\bar{1}$ (Table S1†). The good crystallinity and phase purity of **VMOC-6** and **VMOC-7** were demonstrated by comparing the two powder X-ray diffraction (PXRD) patterns obtained experimentally and calculated from single crystal data (Fig. S4†).

The six $\{VO_6\}$ octahedra form a ring in an edge-sharing pattern and a $\{XO_4\}$ (X = S/V) tetrahedron is coordinated to the center of the unit in an angle-sharing pattern, and the sulfate at the edge is replaced by a C atom from the carboxylic acid to form a concave trigonal "3-pyramidal" MBB $[V_6O_6(OCH_3)_9(XO_4)(COO)_3]^{n-}$ (X = S, n = 2; X = V, n = 1) (abbreviated as $\{V_6(XO_4)$

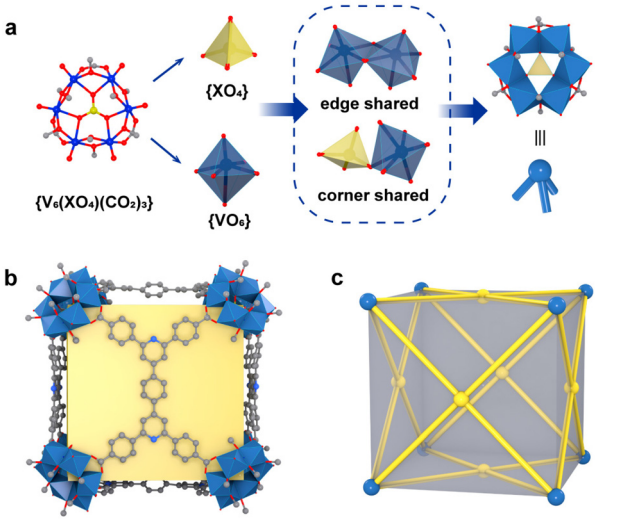

Fig. 2 (a) Structure of $\{V_6(XO_4)(CO_2)_3\}$ (X = S/V) and the coordination mode. The six edge-sharing $\{VO_6\}$ octahedra share the $\{XO_4\}$ tetrahedral vertices to form the "3-pyramidal" MBB. (b) Structures of **VMOC-6** and **VMOC-7**. (c) The simplified cubic model, with the yellow part of H_4PBPTA simplified to "4-planar" and the blue part of the hexanuclear vanadium cluster simplified to "3-pyramidal".

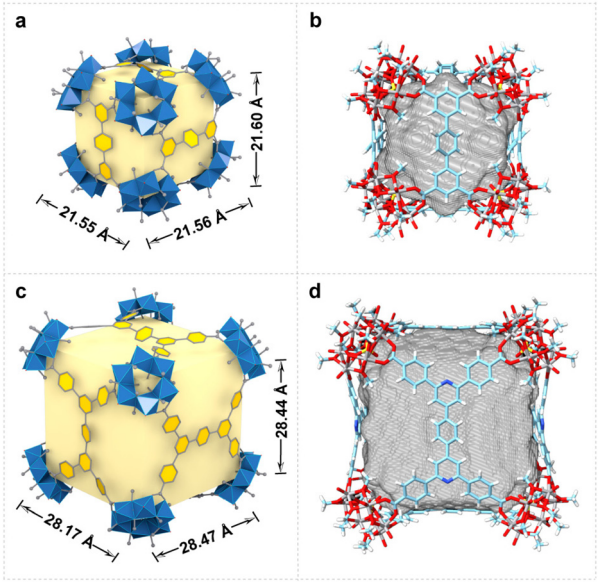

Fig. 3 Crystal structures of **VMOC-4** (a and b) and **VMOC-6** (c and d). The left column highlights the overall size of each cubic cage and the arrangement of the ligands, while the right column shows the void spaces (gray mesh) calculated using the VOIDOO program.

$(CO_2)_3\}$) (Fig. 2a and Fig. S5†). Eight such concave $\{V_6(XO_4)(CO_2)_3\}$ MBBs are connected by six PBPTA ligands to form a discrete metal–organic cube with the V_8F_6 geometry and with O_h symmetry, where the MBBs serve as vertices and PBPTAs serve as faces (Fig. 2b and c). The general formula of the anionic structures of **VMOC-6** and **VMOC-7** can be expressed as $[(V_6O_6(OCH_3)_9(XO_4))_8(BPTC)_6]^{n-}$ (X = S, n = 16; X = V, n = 24). The negative charge is balanced by the corresponding amount of the dimethylamine cation $[NH_2Me_2]^+$ generated by DMF decomposition.

In the structures of **VMOC-6** and **VMOC-7**, the dihedral angle (φ) between two adjacent planes formed by connecting four carboxyl carbon atoms of the tetracarboxylic acid ligands one after another of a cube is close to 90° (Fig. S6†) and the angle (η) between the links is close to 60°, which are consistent with the expected values for the cubes constructed using the face-directed strategy (Table S2†). Compared to that of the reported largest cube **VMOC-4** (21.55 × 21.56 × 21.60 Å^3), the outer diameter (measured from the distance between the outermost carbon atoms of antipodal vertices) of **VMOC-6** and **VMOC-7** reached 28.47 × 28.17 × 28.44 Å^3 due to the expansion of the width of the bridging ligands (Fig. 3a and 3c). To compare the internal space of **VMOC-4** and **VMOC-6**, their internal cavity volumes were calculated from the crystal structure using the VOIDOO program.[31] The internal cavity volume of **VMOC-6** is 7785.657 Å^3, which is 3.2 times larger than that of **VMOC-4** (2437.828 Å^3, Fig. 3b and d). Unfortunately, due to weak supramolecular interactions between the cages and also larger cavities, **VMOP-6** and **VMOP-7** were not stable after solvent removal and exhibited lower adsorption capacity for N_2 (Fig. S7†).[24,32,33]

Iodine vapor uptake

Iodine (I_2) is a volatile and radioactive by-product of nuclear energy production, and its effective capture is particularly important because of its long isotopic lifetime, which directly affects human metabolic processes. It is widely known that I_2 is an electron acceptor, and therefore, it can form host–guest charge transfer complexes with cages containing electron donor groups, which can bind iodine molecules in the cavity. Considering that the structures of **VMOC-6** and **VMOC-7** contain large internal cavities and active site ligands, their potential application in iodine capture was compared to that of **VMOC-4**. Simulating typical nuclear waste reprocessing conditions, samples were placed in glass tubes and transferred to large sealed glass vials containing iodine with no direct contact between the solid samples and the iodine (Fig. S8†). Next, the closed containers were placed under ambient pressure and heated in an oven at 75 °C. As the reaction time increased, the iodine loading increased and was weighed at hourly intervals. Afterwards, the glass vials were placed back into the closed containers and the iodine adsorption was continued until the weight of the sample no longer changed and the adsorption equilibrium was reached. After iodine vapor capture, the iodine uptake capacity was calculated according to eqn (1):

$$Q = (m_2 - m_1)/m_1 \quad (1)$$

where Q (g g^{-1}) is the iodine uptake capacity of the sample, and m_1 (g) and m_2 (g) are the masses of the samples before and after iodine capture, respectively. During iodine capture, the color of the compounds exposed to I_2 vapor gradually darkened with time, indicating the successful adsorption of I_2 (Fig. 4a). Overall, **VMOC-4** first saturated at 6 h of iodine

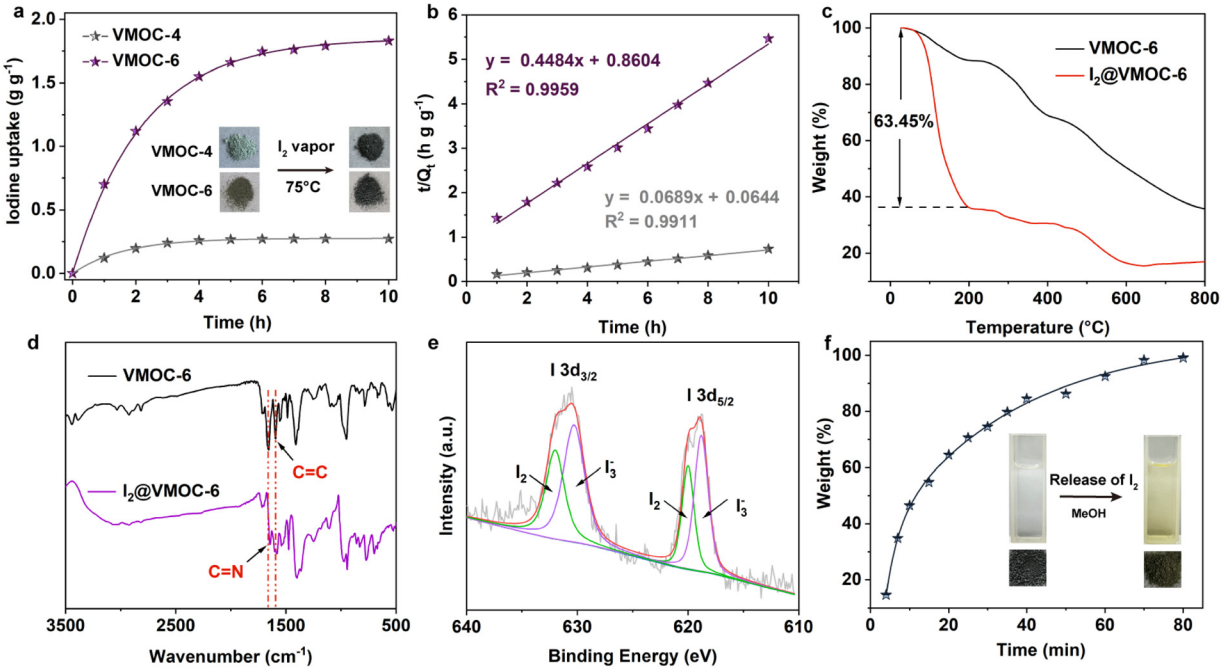

Fig. 4 (a) Iodine vapor adsorption *versus* time for **VMOC-4** and **VMOC-6** at 75 °C and 1 atm (inset: photos of samples before and after I_2 vapor adsorption). (b) The pseudo-second-order kinetic data of the iodine adsorption by **VMOC-4** and **VMOC-6**. (c) TGA curves of **VMOC-6** (black line) and I_2@**VMOC-6** (red line). (d) FT-IR spectra of **VMOC-6** (black line) and I_2@**VMOC-6** (purple line). (e) XPS spectra of I 3d for I_2@**VMOC-6** derived signals. (f) Iodine release *versus* time (inset: photographs of the methanol solution and sample before and after I_2 release).

adsorption, and then **VMOC-6** and **VMOC-7** also saturated in 10 h. Their equilibrium uptake capacities were 0.27 g g^{-1}, 1.83 g g^{-1} and 1.82 g g^{-1}, respectively, and **VMOC-6** has the same adsorption capacity as **VMOC-7** and it is 6.8 times that of **VMOC-4** (Fig. S9†). Since the adsorption curves of **VMOC-6** and **VMOC-7** had basically the same trend, the kinetic data of **VMOC-6** and **VMOC-4** can be analyzed according to a pseudo-second-order kinetic model (Fig. 4b), which can be described using eqn (2):

$$\frac{t}{Q_t} = \frac{1}{kQ_e^2} + \frac{t}{Q_e} \quad (2)$$

where t is the adsorption time (h) and Q_e and Q_t (mg g^{-1}) are the amounts of iodine loaded at equilibrium and at time t, respectively. k (g mg^{-1} h^{-1}) is the pseudo-second-order rate constant for adsorption. The high correlation coefficients (R^2 > 0.99) obtained indicate that the uptake of iodine by **VMOC-6** and **VMOC-4** conforms to a pseudo-second-order kinetic model with rate constants of 0.4484 and 0.0689 g mg^{-1} h^{-1}, respectively. Further thermogravimetric tests were performed on **VMOC-6** before and after iodine uptake, and the TGA curve of I_2@**VMOC-6** after iodine uptake showed a significant mass loss before 200 °C compared to that of **VMOC-6**, which was due to the release of captured iodine. The loss attributed to iodine was estimated to be 63.45% of the total weight, which coincided with the iodine content of I_2@**VMOC-6** (64.15%) (Fig. 4c). To the best of our knowledge, studies on the adsorption of iodine vapor by metal–organic polyhedra are relatively rare.[34] **VMOC-6** has the highest iodine adsorption capacity among MOPs[34] and surpasses most MOFs[35] (Table S3†), such as the well-known ZIF-8 (1.25 g g^{-1}),[36] Uio-66 (1.17 g g^{-1})[37] and HKUST-1 (1.75 g g^{-1}).[38]

To investigate the determinants of iodine capture, scanning electron microscopy (SEM), energy dispersive X-ray spectroscopy (EDS) mapping, Fourier transform infrared (FTIR) analysis, and X-ray photoelectron spectroscopy (XPS) were applied for characterization. SEM images showed that the prepared **VMOC-6** cubes were rhombic crystals with no change in morphology after iodine adsorption. The EDS mapping patterns showed that iodine was uniformly distributed throughout **VMOC-6** after iodine adsorption (Fig. S10†). Further study by FTIR spectroscopy revealed that the C=N band of **VMOC-6** shifted from 1657 cm^{-1} to 1645 cm^{-1} after iodine loading and the C=C stretching vibration also changed, indicating that the adsorption sites may be distributed on the benzene and pyridine rings of the ligand (Fig. 4d).[39] As shown in Fig. 4e, in the I 3d XPS spectrum, two distinct peaks of I_2@**VMOC-6** are located at 620.0 and 632.0 eV, attributed to I $3d_{5/2}$ and I $3d_{3/2}$ of the I_2 molecule, respectively, and the other two peaks are located at 618.6 and 630.3 eV, attributed to I_3^-, indicating that the adsorbed iodine species are present in the I_2 and I_3^- forms. Examples of iodine adsorption using redox metals in some MOFs exist,[40,41] and the XPS characterization of I_2@**VMOC-6** considering the redox properties of vanadium revealed the presence of V^V, suggesting that some of the V^{IV} was reduced to V^V (Fig. S11†). Thus, it was demonstrated that **VMOC-6** and iodine have a driving force for adsorption, prob-

ably due to the weak π–π interactions between the pyridine ring and iodine. Moreover, N acts as a molecular trap for iodine due to its strong affinity for iodine.[42,43] Notably, it is due to two processes, charge transfer between I_2 and the nitrogen atoms in the pyridine ring and redox reactions between I_2 and V, that the adsorbed iodine in **VMOC-6** can be further converted into the polyiodide anion (I_3^-).[44,45] This indicates that the capture process is a combination of physical and chemical adsorption. Therefore, the high iodine uptake capacity of **VMOC-6** can be attributed to the synergistic effect of the larger internal space, the high affinity of the pyridine-containing donor for iodine and the redox activity of V.

The captured iodine can be released from I_2@**VMOC-6** through contact with a suitable solvent (*e.g.* MeOH). The iodine release process from I_2@**VMOC-6** in methanol solution was observed using a UV spectrophotometer at ambient temperature. When 2 mg of the I_2@**VMOC-6** solid was immersed in MeOH, the captured iodine continuously released and the color of the solution changed from colorless to pale yellow (Fig. 4f). The UV-vis spectrum of the methanol solution showed two bands at 291 and 360 nm and a shoulder at 439 nm (Fig. S12†), which was attributed to the presence of the polyiodide anion in I_2@**VMOC-6**.[46–49] The amount of iodine released was calculated from the UV-vis spectral data and the corresponding standard working curve of the I_2 methanol solution (Fig. S13†). The time-dependent profile of I_2@**VMOC-6** in methanol showed that about 84.5% of the captured iodine rapidly released in the first 40 min, after which the release rate of iodine gradually decreased with almost complete release of iodine at 80 min (Fig. 4f).

Iodine adsorption in solution

Encouraged by its excellent performance in iodine vapor capture, the I_2 adsorption capacity of **VMOC-6** in solution was investigated. As nonpolar iodine is insoluble in polar solvents such as water, cyclohexane was chosen as the solvent for the adsorption experiments and the iodine concentration in the solution was determined by UV-vis spectrometry. The standard curve of iodine in cyclohexane solution obtained using UV-vis spectroscopy showed a good linear relationship between the absorbance value and the concentration of iodine, satisfying the Beer–Lambert law, as shown in Fig. S14.† It is well known that adsorption equilibrium isotherms can be used to describe the diffusion state of the adsorbent molecules and the adsorbent at equilibrium. Different equilibrium data were collected to determine the amount of iodine uptake *versus* the iodine concentration at equilibrium by varying the amount of adsorbent, that is, by exposing 5–25 mg of **VMOC-6** to a solution of cyclohexane with an iodine concentration of 0.002 mmol L^{-1}. As seen in Fig. 5a, the amount of iodine adsorbed continues to increase as the equilibrium concentration increases. The adsorption isotherms can be simulated using the Langmuir and Freundlich models, where the Langmuir isotherm model assumes that the adsorption process occurs on a homogeneous monolayer surface of the adsorbent, while the Freundlich model assumes that the adsorption occurs at a non-homogeneous surface, as follows:

$$\text{Langmuir model}: Q_e = \frac{Q_m K_L C_e}{1 + K_L C_e} \quad (3)$$

$$\text{Freundlich model}: Q_e = K_F C_e^{\frac{1}{n}} \quad (4)$$

where Q_m and Q_e (mg g^{-1}) are the maximum amount of iodine adsorbed and the amount of iodine adsorbed at equilibrium. C_e (mg L^{-1}) is the concentration of iodine in the cyclohexane solution at adsorption equilibrium. K_L and K_F are the Langmuir and Freundlich constants related to the heat of adsorption and the Freundlich constant indicates the adsorption capacity at an equilibrium concentration equal to 1, and $1/n$ represents the adsorption strength. The corresponding values for the two isotherm models are shown in Table 1. It can be seen from the R^2 values that the Langmuir model fits better than the Freundlich model, which means that the adsorption sites on the **VMOC-6** surface are evenly distributed. Based on the Langmuir model, the saturation adsorption capacity was calculated to be 236.31 mg g^{-1}. The adsorption kinetics of iodine was further investigated by UV-vis monitoring of this adsorption process by immersing the treated 30 mg crystal sample in 35 mL of cyclohexane solution with an iodine concentration of 0.002 mol L^{-1} at room temperature (Fig. 5b).

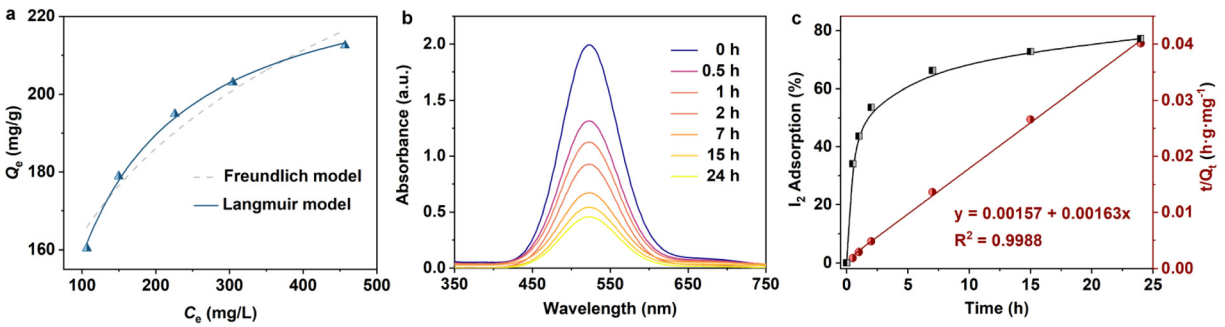

Fig. 5 (a) Langmuir and Freundlich model fitting of the isotherm of iodine adsorption by **VMOC-6** in cyclohexane solution. (b) Time evolution of the UV-vis absorption spectra of cyclohexane solutions in the presence of **VMOC-6**. (c) The kinetics of the adsorption process of iodine on **VMOC-6** was plotted with the relative removal rate (%) of iodine (black line) and t/Q_t (red line) *versus* time.

Table 1 Adsorption equilibrium constants of Langmuir and Freundlich isotherm equations for iodine adsorption on **VMOC-6** adsorbents

Langmuir			Freundlich		
Q_m (mg g^{-1})	K_L (L mg^{-1})	R^2	K_F (mg g^{-1})	n	R^2
236.3066	0.0203	0.9965	70.3633	5.45	0.9392

The concentration of iodine in the solution decreased rapidly with increasing contact time, and the relative removal of iodine reached 53.62% within 2 h. After 24 h, the relative removal of iodine reached 77.26% and the adsorption equilibrium was reached (Fig. 5c). The rapid decrease of iodine concentration in the solution with increasing contact time was accompanied by a change of color from purple to pink. t/Q_t showed a linear relationship with t (R^2 = 0.9988), demonstrating that the kinetic data were in good agreement with the pseudo-secondary kinetic model.

Conclusions

In summary, the tetracarboxylic acid ligand H_4PBPTA was successfully self-assembled with the 3-connected hexanuclear vanadium clusters $\{V_6(SO_4)(CO_2)_3\}$ and $\{V_6(VO_4)(CO_2)_3\}$ to form two isostructural metal–organic cubes **VMOC-6** and **VMOC-7** using the face-directed strategy under solvothermal conditions. They are the largest metal–organic cubes based on metal clusters, with a side length of about 28.3 Å and an inner cavity volume of about 7785.657 Å^3. The presence of electron-donating pyridine groups and redox-active V and the large inner cavity led to an iodine trapping capacity of 1.83 g g^{-1} in the gas phase, which is the highest iodine adsorption capacity of metal–organic polyhedra to date and exceeds that of most previously reported metal–organic frameworks. This study provides a new perspective on the design of metal–organic polyhedra with tunable internal cavities and potential applications in the treatment of iodine-containing nuclear waste.

Conflicts of interest

There are no conflicts to declare.

Acknowledgements

This work was financially supported by the NSFC of China (No. 22271023, 22175033).

References

1 S. R. Seidel and P. J. Stang, High-symmetry coordination cages via self-assembly, *Acc. Chem. Res.*, 2002, **35**, 972–983.
2 T. R. Cook, V. Vajpayee, M. H. Lee, P. J. Stang and K.-W. Chi, Biomedical and Biochemical Applications of Self-Assembled Metallacycles and Metallacages, *Acc. Chem. Res.*, 2013, **46**, 2464–2474.
3 L.-J. Chen, H.-B. Yang and M. Shionoya, Chiral metallosupramolecular architectures, *Chem. Soc. Rev.*, 2017, **46**, 2555–2576.
4 R. Zhang, S. Ji, N. Wang, L. Wang, G. Zhang and J.-R. Li, Coordination-Driven In Situ Self-Assembly Strategy for the Preparation of Metal–Organic Framework Hybrid Membranes, *Angew. Chem., Int. Ed.*, 2014, **53**, 9775–9779.
5 B. H. Northrop, Y.-R. Zheng, K.-W. Chi and P. J. Stang, Self-Organization in Coordination-Driven Self-Assembly, *Acc. Chem. Res.*, 2009, **42**, 1554–1563.
6 Z.-Y. Li, Y. Zhang, C.-W. Zhang, L.-J. Chen, C. Wang, H. Tan, Y. Yu, X. Lo and H.-B. Yang, Cross-Linked Supramolecular Polymer Gels Constructed from Discrete Multi-pillar 5 arene Metallacycles and Their Multiple Stimuli-Responsive Behavior, *J. Am. Chem. Soc.*, 2014, **136**, 8577–8589.
7 Q.-F. Sun, J. Iwasa, D. Ogawa, Y. Ishido, S. Sato, T. Ozeki, Y. Sei, K. Yamaguchi and M. Fujita, Self-Assembled $M_{24}L_{48}$ Polyhedra and Their Sharp Structural Switch upon Subtle Ligand Variation, *Science*, 2010, **328**, 1144–1147.
8 M. Eddaoudi, J. Kim, J. B. Wachter, H. K. Chae, M. O'Keeffe and O. M. Yaghi, Porous metal–organic polyhedra: 25 angstrom cuboctahedron constructed from 12 $Cu_2(CO_2)_4$ paddle-wheel building blocks, *J. Am. Chem. Soc.*, 2001, **123**, 4368–4369.
9 A. C. Sudik, A. R. Millward, N. W. Ockwig, A. P. Cote, J. Kim and O. M. Yaghi, Design, synthesis, structure, and gas (N_2, Ar, CO_2, CH_4, and H_2) sorption properties of porous metal-organic tetrahedral and heterocuboidal polyhedra, *J. Am. Chem. Soc.*, 2005, **127**, 7110–7118.
10 D. J. Tranchemontagne, Z. Ni, M. O'Keeffe and O. M. Yaghi, Reticular Chemistry of Metal–Organic Polyhedra, *Angew. Chem., Int. Ed.*, 2008, **47**, 5136–5147.
11 M. L. Saha, X. Yan and P. J. Stang, Photophysical Properties of Organoplatinum(II) Compounds and Derived Self-Assembled Metallacycles and Metallacages: Fluorescence and its Applications, *Acc. Chem. Res.*, 2016, **49**, 2527–2539.
12 F. J. Rizzuto and J. R. Nitschke, Stereochemical plasticity modulates cooperative binding in a CoII12L_6 cuboctahedron, *Nat. Chem.*, 2017, **9**, 903–908.
13 D. Fiedler, D. H. Leung, R. G. Bergman and K. N. Raymond, Selective molecular recognition, C–H bond activation, and catalysis in nanoscale reaction vessels, *Acc. Chem. Res.*, 2005, **38**, 349–358.
14 S. Lee, H. Jeong, D. Nam, M. S. Lah and W. Choe, The rise of metal–organic polyhedra, *Chem. Soc. Rev.*, 2021, **50**, 528–555.
15 A. Kondinski, A. Menon, D. Nurkowski, F. Farazi, S. Mosbach, J. Akroyd and M. Kraft, Automated Rational Design of Metal–Organic Polyhedra, *J. Am. Chem. Soc.*, 2022, DOI: **10.1021/jacs.2c03402**.
16 W. J. Ramsay, F. T. Szczypinski, H. Weissman, T. K. Ronson, M. M. J. Smulders, B. Rybtchinski and

J. R. Nitschke, Designed Enclosure Enables Guest Binding Within the 4200 Å^3 Cavity of a Self-Assembled Cube, *Angew. Chem., Int. Ed.*, 2015, **54**, 5636–5640.

17 W. J. Ramsay, T. K. Ronson, J. K. Clegg and J. R. Nitschke, Bidirectional Regulation of Halide Binding in a Heterometallic Supramolecular Cube, *Angew. Chem., Int. Ed.*, 2013, **52**, 13439–13443.

18 P. Sutar, V. M. Suresh, K. Jayaramulu, A. Hazra and T. K. Maji, Binder driven self-assembly of metal–organic cubes towards functional hydrogels, *Nat. Commun.*, 2018, **9**, 3587.

19 J. P. Lang, Q. F. Xu, Z. N. Chen and B. F. Abrahams, Assembly of a supramolecular cube, $[CP^*WS_3CU_3]_8CI_8[CN]_{12}Li_4$ from a preformed incomplete cubane-like compound $[PPh_4]$ $[CP^*WS_3(CuCN)_3]$, *J. Am. Chem. Soc.*, 2003, **125**, 12682–12683.

20 A. W. Augustyniak, M. Fandzloch, M. Domingo, I. Lakomska and J. A. R. Navarro, A vanadium(IV) pyrazolate metal-organic polyhedron with permanent porosity and adsorption selectivity, *Chem. Commun.*, 2015, **51**, 14724–14727.

21 Y. Zhang, H. Gan, C. Qin, X. Wang, Z. Su and M. J. Zaworotko, Self-Assembly of Goldberg Polyhedra from a Concave $WV_5O_{11}(RCO_2)_5(SO_4)^{3-}$ Building Block with 5-Fold Symmetry, *J. Am. Chem. Soc.*, 2018, **140**, 17365–17368.

22 Y.-T. Zhang, X.-L. Wang, E.-L. Zhou, X.-S. Wu, B.-Q. Song, K.-Z. Shao and Z.-M. Su, Polyoxovanadate-based organic inorganic hybrids: from $\{V_5O_9Cl\}$ clusters to nanosized octahedral cages, *Dalton Trans.*, 2016, **45**, 3698–3701.

23 H. Gan, N. Xu, C. Qin, C. Sun, X. Wang and Z. Su, Equi-size nesting of Platonic and Archimedean metal-organic polyhedra into a twin capsid, *Nat. Commun.*, 2020, **11**, 4103.

24 Y. Gong, Y. Zhang, C. Qin, C. Sun, X. Wang and Z. Su, Bottom-Up Construction and Reversible Structural Transformation of Supramolecular Isomers based on Large Truncated Tetrahedra, *Angew. Chem., Int. Ed.*, 2019, **58**, 780–784.

25 N. Xu, H. Gan, C. Qin, X. Wang and Z. Su, From Octahedral to Icosahedral Metal-Organic Polyhedra Assembled from Two Types of Polyoxovanadate Clusters, *Angew. Chem., Int. Ed.*, 2019, **58**, 4649–4653.

26 Y.-T. Zhang, X.-L. Wang, S.-B. Li, Y.-R. Gong, B.-Q. Song, K.-Z. Shao and Z.-M. Su, Anderson-like alkoxo-polyoxovanadate clusters serving as unprecedented second building units to construct metal–organic polyhedra, *Chem. Commun.*, 2016, **52**, 9632–9635.

27 Y.-T. Zhang, S.-B. Li, X.-L. Wang, Y.-R. Gong, K.-Z. Shao and Z.-M. Su, Synthesis, structures, and magnetic properties of metal-organic polyhedra based on unprecedented $\{V_7\}$ isopolyoxometalate clusters, *Dalton Trans.*, 2016, **45**, 14898–14901.

28 Y. Gong, C. Qin, Y. Zhang, C. Sun, Q. Pan, X. Wang and Z. Su, Face-Directed Assembly of Molecular Cubes: In Situ Substitution of a Predetermined Concave Cluster, *Angew. Chem., Int. Ed.*, 2020, **59**, 22034–22038.

29 J. M. Breen and W. Schmitt, Hybrid organic-inorganic polyoxometalates: Functionalization of V^{IV}/V^V nanosized clusters to produce molecular capsules, *Angew. Chem., Int. Ed.*, 2008, **47**, 6904–6908.

30 Z. Zhang, W.-Y. Gao, L. Wojtas, Z. Zhang and M. J. Zaworotko, A new family of anionic organic–inorganic hybrid doughnut-like nanostructures, *Chem. Commun.*, 2015, **51**, 9223–9226.

31 G. J. Kleywegt and T. A. Jones, Detection, delineation, measurement and display of cavities in macromolecular structures, *Acta Crystallogr., Sect. D: Biol. Crystallogr.*, 1994, **50**, 178–185.

32 D. Luo, X. P. Zhou and D. Li, Beyond Molecules: Mesoporous Supramolecular Frameworks Self-Assembled from Coordination Cages and Inorganic Anions, *Angew. Chem., Int. Ed.*, 2015, **54**, 6190–6195.

33 A. J. Gosselin, C. A. Rowland and E. D. Bloch, Permanently Microporous Metal–Organic Polyhedra, *Chem. Rev.*, 2020, **120**, 8987–9014.

34 W.-Y. Pei, J. Yang, H. Wu, W. Zhou, Y.-W. Yang and J.-F. Ma, A calix 4 resorcinarene-based giant coordination cage: controlled assembly and iodine uptake, *Chem. Commun.*, 2020, **56**, 2491–2494.

35 X. Zhang, J. Maddock, T. M. Nenoff, M. A. Denecke, S. Yang and M. Schroder, Adsorption of iodine in metal–organic framework materials, *Chem. Soc. Rev.*, 2022, **51**, 3243–3262.

36 D. F. Sava, M. A. Rodriguez, K. W. Chapman, P. J. Chupas, J. A. Greathouse, P. S. Crozier and T. M. Nenoff, Capture of Volatile Iodine, a Gaseous Fission Product, by Zeolitic Imidazolate Framework-8, *J. Am. Chem. Soc.*, 2011, **133**, 12398–12401.

37 J. Maddock, X. Kang, L. Liu, B. Han, S. Yang and M. Schröder, The Impact of Structural Defects on Iodine Adsorption in UiO-66, *Chemistry)*, 2021, **3**, 525–531.

38 D. F. Sava, K. W. Chapman, M. A. Rodriguez, J. A. Greathouse, P. S. Crozier, H. Zhao, P. J. Chupas and T. M. Nenoff, Competitive I_2 Sorption by Cu-BTC from Humid Gas Streams, *Chem. Mater.*, 2013, **25**, 2591–2596.

39 D. Luo, Y. He, J. Tian, J. L. Sessler and X. Chi, Reversible Iodine Capture by Nonporous Adaptive Crystals of a Bipyridine Cage, *J. Am. Chem. Soc.*, 2022, **144**, 113–117.

40 H. J. Choi and M. P. Suh, Dynamic and Redox Active Pillared Bilayer Open Framework: Single-Crystal-to-Single-Crystal Transformations upon Guest Removal, Guest Exchange, and Framework Oxidation, *J. Am. Chem. Soc.*, 2004, **126**, 15844–15851.

41 X. Zhang, I. Da Silva, R. Fazzi, A. M. Sheveleva, X. Han, B. F. Spencer, S. A. Sapchenko, F. Tuna, E. J. L. McInnes, M. Li, S. Yang and M. Schröder, Iodine Adsorption in a Redox-Active Metal–Organic Framework: Electrical Conductivity Induced by Host–Guest Charge-Transfer, *Inorg. Chem.*, 2019, **58**, 14145–14150.

42 D. K. L. Harijan, V. Chandra, T. Yoon and K. S. Kim, Radioactive iodine capture and storage from water using magnetite nanoparticles encapsulated in polypyrrole, *J. Hazard. Mater.*, 2018, **344**, 576–584.

43 F. Yu, Y. Chen, Y. Wang, C. Liu and J. Qin, Synthesis of metal-organic framework nanocrystals immobilized with

3D flowerlike Cu-Bi-layered double hydroxides for iodine efficient removal, *J. Mater. Res.*, 2020, **35**, 299–311.

44 X. Liu, A. Zhang, R. Ma, B. Wu, T. Wen, Y. Ai, M. Sun, J. Jin, S. Wang and X. Wang, Experimental and theoretical insights into copper phthalocyanine-based covalent organic frameworks for highly efficient radioactive iodine capture, *Chin. Chem. Lett.*, 2022, **33**, 3549–3555.

45 K. Su, W. Wang, B. Li and D. Yuan, Azo-Bridged Calix 4 resorcinarene-Based Porous Organic Frameworks with Highly Efficient Enrichment of Volatile Iodine, *ACS Sustainable Chem. Eng.*, 2018, **6**, 17402–17409.

46 X. Li, H. Xiong and Q. Jia, A Versatile Solvent-Induced Polymerization Strategy To Synthesize Free-Standing Porous Polymer Nanosheets and Nanotubes for Fast Iodine Capture, *ACS Appl. Mater. Interfaces*, 2019, **11**, 46205–46211.

47 Y. Liao, J. Weber, B. M. Mills, Z. Ren and C. F. J. Faul, Highly Efficient and Reversible Iodine Capture in Hexaphenylbenzene-Based Conjugated Microporous Polymers, *Macromolecules*, 2016, **49**, 6322–6333.

48 T. Geng, S. Ye, Z. Zhu and W. Zhang, Triazine-based conjugated microporous polymers with N,N,N′,N’-tetraphenyl-1,4-phenylenediamine,1,3,5-tris(diphenylamino)benzene and 1,3,5-tris (3-methylphenyl)-phenylamino benzene as the core for high iodine capture and fluorescence sensing of o-nitrophenol, *J. Mater. Chem. A*, 2018, **6**, 2808–2816.

49 H. J. Choi and M. P. Suh, Dynamic and redox active pillared bilayer open framework: Single-crystal-to-single-crystal transformations upon guest removal, guest exchange, and framework oxidation, *J. Am. Chem. Soc.*, 2004, **126**, 15844–15851.